PERGAMON

International Journal of Plasticity 18 (2002) 661–686

INTERNATIONAL JOURNAL OF Plasticity

www.elsevier.com/locate/ijplas

A model of large-strain cyclic plasticity describing the Bauschinger effect and workhardening stagnation

Fusahito Yoshida*, Takeshi Uemori

Department of Mechanical Systems Engineering, Hiroshima University 1-4-1, Kagamiyama, Higashi-Hiroshima 739-8527, Japan

Received in final revised form 1 May 2001

Abstract

This paper presents a constitutive model that has a high capability of describing the deformation behavior of large-strain cyclic plasticity and also the stress–strain responses at small-scale re-yielding after large prestrain. A new equation of backstress evolution is proposed for an accurate simulation of the transient Bauschinger effect. Furthermore, an original idea of a non-isotropic-hardening surface defined in the stress space is presented for the description of the workhardening stagnation appearing under reverse deformation, as well as the strain-range and mean-strain dependencies of cyclic hardening characteristics. The validity of this model is confirmed by comparing the cyclic stress–strain responses calculated by the model with the experimental observations on some steel sheets and an aluminum sheet.

Keywords: B. Cyclic loading; B. Constitutive behaviour; B. Finite strain; Bauschinger effect

1. Introduction

Elastic–plastic deformation behavior under cyclic loading has been investigated for some decades, and many constitutive models of cyclic plasticity have been proposed. However, most of the discussions on cyclic plasticity models were within theories of infinitesimal deformation, since these research works were mainly aimed at using the models for structural analyses of low-cycle fatigue or thermal fatigue. Recently, in the field of sheet metal forming, some researchers pointed out that in some cases the Bauschinger effect should be taken into account for the accurate

* Corresponding author. Tel.: +81-824-24-7541; fax: +81-824-22-7193.
E-mail address: yoshida@mec.hiroshima-u.ac.jp (F. Yoshida).

0749-6419/02/$ - see front matter
PII: S0749-6419(01)00050-X

prediction of springback (e.g. Uemori et al., 1998, 2000; Besdo, 2000; Wagoner et al., 2000). Obviously, sheet metal forming is a typical large-strain problem, and the springback is a process of small-scale re-yielding after large prestrain. Therefore, for constitutive modeling, we should pay much attention to the deformation behavior of large-strain cyclic plasticity and also the stress–strain responses at small-scale re-yielding after large prestrain.

As for experimental observations, only a limited number of papers have been published on large-strain cyclic plasticity (e.g. Wilson and Bate, 1986; Hu, 1994), while there are many papers on reverse deformation experiments after large strains (e.g. Hasegawa and Yakou, 1975; Christodoulou et al., 1986; Stout and Rollett, 1990; Takahashi and Shiono, 1991; Hu et al., 1992; Kuwabara et al., 1995; Khan and Jackson, 1999; Miller et al., 1999). One of the reasons for the situation is that the motivation for large-strain cyclic plasticity arose only recently in the field of sheet metal forming simulations (e.g. PAM-STAMP^{TM}, 2000). It is also due to the difficulties in experimental techniques for subjecting sheet metals to cyclic deformation at large strain. Recently, the present authors (Yoshida et al., 2001) succeeded in performing experiments of in-plane cyclic tension–compression deformation of sheet metals at large strain, by using adhesively bonded sheet specimens and a special device for preventing the buckling of the specimens. From the experiments on a mild steel sheet and a dual-phase steel sheet, we found the following deformation characteristics:

a. During reverse deformation, *the transient Bauschinger deformation,* characterized by an early re-yielding and smooth elastic–plastic transition with a rapid change of workhardening rate, is followed by the plastic deformation with an apparent *permanent softening*.
b. For the mild steel sheet, abnormal shapes of reverse stress–strain curves appear due to the workhardening stagnation. In contrast, for the high strength steel, they are not visible.
c. Cyclic stress amplitudes strongly depend on cyclic strain ranges, as well as the mean strains. The larger the strain ranges, the larger the saturated stress amplitudes.
d. For both steels, Young's moduli decrease in the state of unloading with increasing prestrain.

The present authors also pointed out that a classical constitutive model of mixed isotropic–kinematic hardening [termed 'IH + NLK model' which is the simplest form of the Chaboche and Rousselier model (1983)], which has been released in widely distributed commercial FE-codes (Anon., 1997; PAM-STAMP^{TM}, 2000), cannot describe some of the above deformation characteristics, especially the reproduction of the workhardening stagnation is completely impossible. Even if we add a linear component to the IH + NLK model (termed 'IH + NLK + LK model'), it is still hardly possible to predict the behaviors (b) and (c). As for the prestrain dependency of Young's moduli mentioned in (d), none of constitutive models has so far theoretically indicated, and it could be expressed only by a certain empirical model (e.g. Yoshida et al., 2001).

Hu et al. (1992) and Hu (1994) have proposed a uniaxial constitutive model of large-strain plasticity that can describe the workhardening stagnation, as well as the cyclic strain-range dependency of stress amplitude. Later, Teodosiu et al. (1997) generalized the model for multiaxial plasticity. Although these models can simulate the transient Bauschinger effect, as well as the behavior of workhardening stagnation, it seems that they did not pay much attention to the accurate description of the stress–strain responses in the small-scale re-yielding region, which is essential for the springback prediction. In their models, the evolution equations for three internal variables (two of them are associated with the physical background of directional strength and the polarity of persistent dislocation structures and the one is the backstress) are so complicated that identifying all the material parameters from experimentally obtained stress–strain curves would be difficult [e.g. Teodosiu et al.'s (1997) model involves 10 parameters].

In the present paper, we propose a new constitutive model of large-strain cyclic plasticity that has a high capability of describing the above-mentioned cyclic deformation characteristics. This is a two-surface model that assumes the kinematic hardening of the yield surface within the bounding surface of mixed isotropic–kinematic hardening. In the modeling, we paid much attention to simulate precisely the behavior of the transient Bauschinger effect, as well as global cyclic hardening characteristics such as strain-range dependent cyclic hardening and workhardening stagnation. It should be emphasized that in this model we have introduced the following two new ideas:

- a backstress evolution equation to express more realistic shape of a reverse stress–strain curve in the period of the transient Bauschinger deformation, and
- a non-isotropic-hardening (hereafter called 'non-IH' for brevity) surface defined in the stress space to describe the workhardening stagnation, but not in the plastic strain space like Chaboche et al. (1979) and Ohno (1982).

This model has an advantage in the material parameter identification. Most of the parameters (seven parameters in the basic version of this model) can be easily determined directly from the experimentally obtained stress–strain curves. The validity of this model is confirmed in the present paper by comparing the numerical simulations of stress–strain responses with our experimental results on two types of steel sheets under various cyclic deformations. Also compared is the experimental data of reverse deformations on an aluminium sheet reported by Kuwabara et al. (1995).

2. Constitutive modeling

2.1. Framework of the model

With the assumption of a small elastic and large plastic deformation, the rate of deformation $\mathbf{D}$ is decomposed as

$$\mathbf{D} = \mathbf{D}^{\mathrm{e}} + \mathbf{D}^{\mathrm{p}}, \tag{1}$$

where $\mathbf{D}^{\mathrm{e}}$ and $\mathbf{D}^{\mathrm{p}}$ are the elastic and plastic parts of the rate, respectively. The decomposition of the continuum spin $\mathbf{W}$ is given by

$$\mathbf{W} = \mathbf{\Omega} + \mathbf{W}^{\mathrm{p}}, \tag{2}$$

where $\mathbf{W}^{\mathrm{p}}$ denotes the plastic spin and $\mathbf{\Omega}$ is the spin of substructures (Dafalias, 1985). The constitutive equation of elasticity is expressed by the equation:

$$\mathring{\boldsymbol{\sigma}} = \dot{\boldsymbol{\sigma}} - \mathbf{\Omega}\boldsymbol{\sigma} + \boldsymbol{\sigma}\mathbf{\Omega} = \mathbf{C} : \mathbf{D}^{\mathrm{e}}, \tag{3}$$

where $\boldsymbol{\sigma}$ and $\mathring{\boldsymbol{\sigma}}$ are the Cauchy stress and its objective rate, and $\mathbf{\Omega}$ is the elasticity modulus tensor. Here, $(\circ)$ stands for the objective rate.

The present constitutive model of plasticity has been constructed within the framework of well-known two-surface modeling, wherein the yield surface moves kinematically within a bounding surface (e.g. Krieg, 1975; Dafalias and Popov, 1976). Since the experimental stress–strain responses under reverse deformation show that the re-yielding starts at a very early stage of stress reversal (Yoshida et al., 2001), we assume only the kinematic hardening for the yield surface, while for the bounding surface mixed isotropic–kinematic hardening, as schematically shown in Fig. 1. Based on the von Mises criterion, the yield function f and the associated flow rule are given by the equations:

$$f = \frac{3}{2}(\mathbf{s} - \boldsymbol{\alpha}) : (\mathbf{s} - \boldsymbol{\alpha}) - Y^2 = 0, \tag{4a}$$

$$\mathbf{D}^{\mathrm{p}} = \frac{\partial f}{\partial \mathbf{s}}\dot{\lambda}, \tag{4b}$$

where $\mathbf{s}$ and $\boldsymbol{\alpha}$ denote the Cauchy stress deviator and the backstress deviator, respectively, and Y is the radius of the yield surface in the deviatoric stress space. The bounding surface F is expressed by the equation:

$$F = \frac{3}{2}(\mathbf{s} - \boldsymbol{\beta}) : (\mathbf{s} - \boldsymbol{\beta}) - (B + R)^2 = 0, \tag{5}$$

where $\boldsymbol{\beta}$ denotes the center of the bounding surface, and B and R are its initial size and isotropic hardening (IH) component. The motion of the yield surface within the bounding surface under uniaxial forward-reverse deformation is schematically depicted in Fig. 2(a). The mixed isotropic–kinematic hardening of the bounding surface is also schematically illustrated in Fig. 2(b).

The kinematic hardening of the yield surface describes the transient Bauschinger deformation characterized by early re-yielding and the subsequent rapid change of workhardening rate, which is mainly due to the motion of less stable dislocations, such as piled-up dislocations. The isotropic hardening of the bounding surface represents the global workhardening, which is associated with the formation of stable dislocation structures, such as cell walls. The permanent softening and workhardening

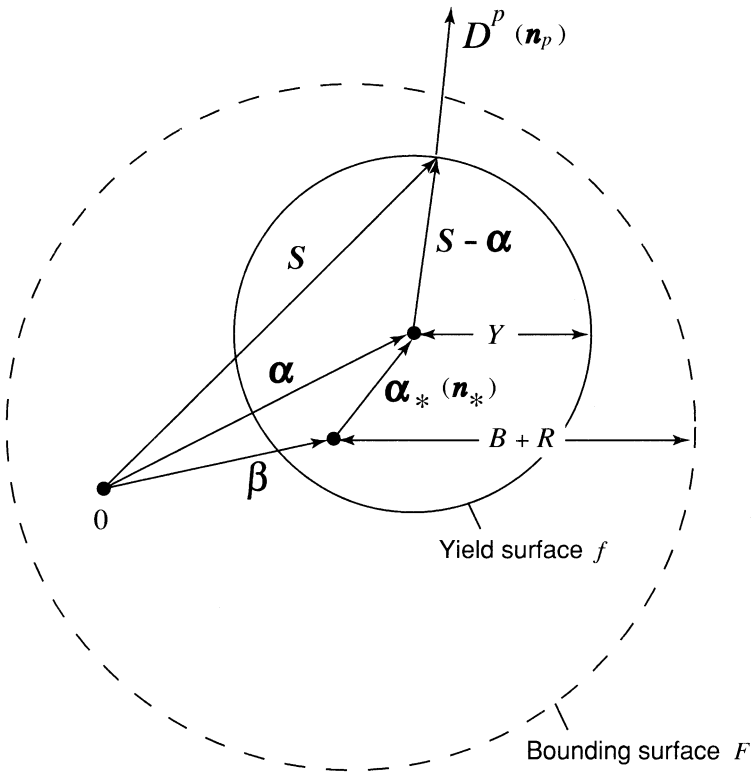

Fig. 1. Schematic illustration of the two-surface model.

stagnation is caused by the dissolution of dislocation cell walls preformed during forward deformation and the formation of new dislocation microstructures during reverse deformation (e.g. Hasegawa-Yakou, 1975; Christodoulou et al., 1986). In order to describe such deformation characteristics under stress reversals, the kinematic hardening and non-IH region during stress reversals are assumed for the bounding surface.

The model is developed taking account of users' requirement for a limited number of the material parameters and also the clear scheme of parameter identification.

2.2. Kinematic hardening of the yield surface

The relative kinematic motion of the yield surface with respect to the bounding surface is expressed by

$$\boldsymbol{\alpha}_* = \boldsymbol{\alpha} - \boldsymbol{\beta}. \tag{6}$$

For the evolution of $\boldsymbol{\alpha}_*$, let us begin our discussion with the well-known Armstrong and Frederick (1966) rule (hereafter we call 'AF model'):

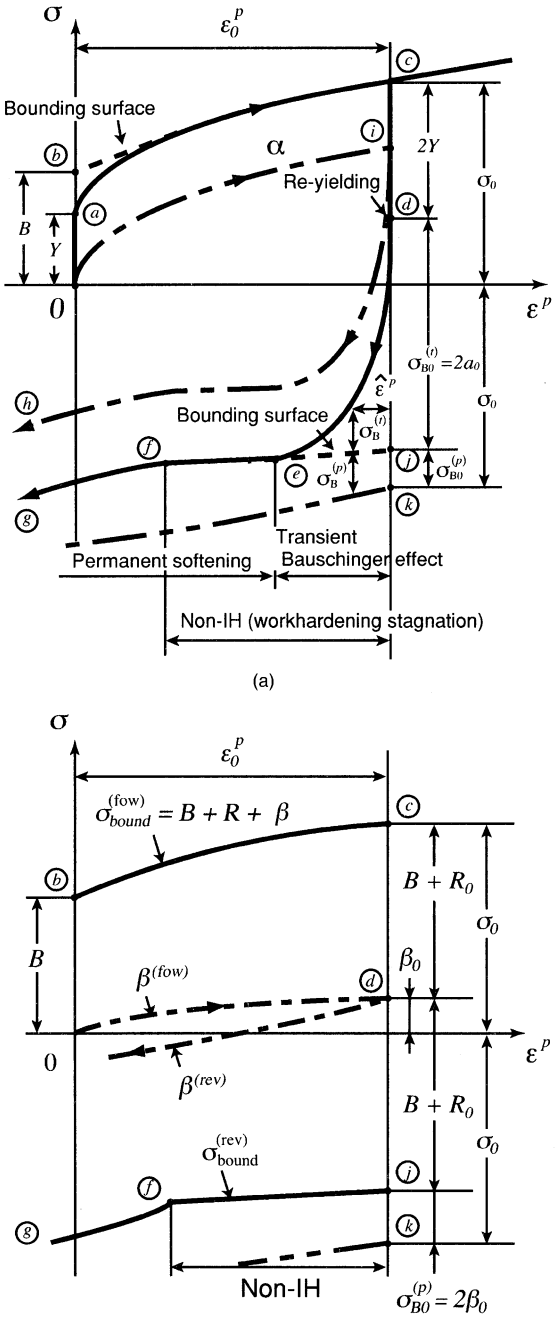

Fig. 2. Schematic illustrations of the motion of: (a) the yield surface; and (b) the bounding surface under a uniaxial forward–reverse deformation.

$$\mathring{\boldsymbol{\alpha}}_* = C\left(\frac{2}{3}a\mathbf{D}^{\mathrm{p}} - \boldsymbol{\alpha}_*\dot{p}\right) = \sqrt{\frac{2}{3}}Ca\dot{p}\left[\mathbf{n}_{\mathrm{p}} - \left(\frac{\bar{\alpha}_*}{a}\mathbf{n}_*\right)\right], \tag{7a}$$

$$\dot{p} = \sqrt{(2/3)\mathbf{D}^{\mathrm{p}} : \mathbf{D}^{\mathrm{p}}}, \quad \bar{\alpha}_* = \sqrt{\frac{3}{2}\boldsymbol{\alpha}_* : \boldsymbol{\alpha}_*}, \quad a = B + R - Y, \tag{7b}$$

where $\dot{p}$ is the effective plastic strain rate, $\mathbf{n}_{\mathrm{p}}$ and $\mathbf{n}_*$ denote the unit vectors in the directions of $\mathbf{D}^{\mathrm{p}}$ and $\boldsymbol{\alpha}_*$, respectively, and C is a material parameter that controls the rate of the kinematic hardening. Although there are several discussions on the plastic spins and the objective stress rates (e.g. Dafalias, 1985; Zbib and Aifantis, 1988; Dafalias and Rashid, 1989; Van der Gissen, 1991; Kuroda, 1996; Diegele et al., 2000), we may simply assume that all structural variables turn with the same spin $\boldsymbol{\Omega}$, e.g. $\mathring{\boldsymbol{\alpha}}_* = \dot{\boldsymbol{\alpha}}_* - \boldsymbol{\Omega}\,\boldsymbol{\alpha}_* + \boldsymbol{\alpha}_*\boldsymbol{\Omega}$. Furthermore, since the effect of plastic spin on the stress-strain responses is not so significant at a moderately large strain, we may use the continuum spin $\mathbf{W}$ instead of $\boldsymbol{\Omega}$ in such a case.

Instead of the AF model, Burlet and Cailleteaud (1987) proposed the following backstress evolution, whose finite plasticity expression is

$$\mathring{\boldsymbol{\alpha}}_* = C\left(\frac{2}{3}a - \sqrt{\frac{2}{3}}\boldsymbol{\alpha}_* : \mathbf{n}_{\mathrm{p}}\right)\mathbf{D}^{\mathrm{p}} = \sqrt{\frac{2}{3}}Ca\dot{p}\left[1 - \left(\frac{\bar{\alpha}_*}{a}\right)\mathbf{n}_* : \mathbf{n}_{\mathrm{p}}\right]\mathbf{n}_{\mathrm{p}}, \tag{8}$$

The above two evolution equations are identical in a uniaxial stress state, as given by the equation:

$$\dot{\alpha}_* = C(a\dot{\varepsilon}^{\mathrm{p}} - \alpha_*|\dot{\varepsilon}^{\mathrm{p}}|), \tag{9}$$

where $\dot{\varepsilon}^{\mathrm{p}}$ is the uniaxial plastic strain rate. From this evolution equation, the transient stress offset, $\sigma_{\mathrm{B}}^{(\mathrm{t})}$ which is defined as the difference between the reverse stress–strain curve [(d)–(e) in Fig. 2(a)] and the extrapolated curve of the region of permanent softening [(e)–(j) in Fig. 2(a)], is given by

$$\sigma_{\mathrm{B}}^{(\mathrm{t})} = a + \alpha_* \approx 2a\mathrm{e}^{-C\hat{\varepsilon}^{\mathrm{p}}}, \tag{10}$$

where $\hat{\varepsilon}^{\mathrm{p}}$ is the reverse plastic strain. As will be discussed later, this equation puts too much constraint on the shape of stress–strain curve of the transient Bauschinger deformation. Therefore, we introduce a more flexible form of the backstress evolution, as

$$\dot{\alpha}_* = Ca\left[\dot{\varepsilon}^{\mathrm{p}} - \mathrm{sgn}(\alpha_*)\left(\frac{|\alpha_*|}{a}\right)^{\gamma}|\dot{\varepsilon}^{\mathrm{p}}|\right]. \tag{11}$$

Here, γ is a material parameter, and in the special case of $\gamma = 1$, Eq. (11) yields Eq. (9). For multiaxial stress state, Eq. (11) is generalized either based on the AF model [Eq. (7)], as

$$\mathring{\boldsymbol{\alpha}}_* = \sqrt{\frac{2}{3}} Ca\dot{p}\left[\mathbf{n}_\mathrm{p} - \left(\frac{\bar{\alpha}_*}{a}\right)^{\gamma}\mathbf{n}_*\right], \tag{12}$$

or based on the Burlet–Cailleteaud model [Eq. (8)], as

$$\mathring{\boldsymbol{\alpha}}_* = \sqrt{\frac{2}{3}} Ca\dot{p}\left[1 - \left(\frac{\bar{\alpha}_*}{a}\right)^{\gamma}\mathbf{n}_* : \mathbf{n}_\mathrm{p}\right]\mathbf{n}_\mathrm{p}, \tag{13}$$

From our experimental observations on two types of steel sheets (Yoshida et al., 2001), we have concluded that $\gamma = 0.5$ gives a good approximation to the real stress–strain responses, then

$$\mathring{\boldsymbol{\alpha}}_* = \sqrt{\frac{2}{3}} Ca\dot{p}\left(\mathbf{n}_\mathrm{p} - \sqrt{\frac{\bar{\alpha}_*}{a}}\mathbf{n}_*\right), \tag{14}$$

or

$$\mathring{\boldsymbol{\alpha}}_* = \sqrt{\frac{2}{3}} Ca\dot{p}\left(1 - \sqrt{\frac{\bar{\alpha}_*}{a}}\mathbf{n}_* : \mathbf{n}_\mathrm{p}\right)\mathbf{n}_\mathrm{p}, \tag{15}$$

Under the uniaxial stress state, the above Eqs. (14) and (15) yield

$$\dot{\alpha}_* = Ca\left(\dot{\varepsilon}^\mathrm{p} - \mathrm{sgn}(\alpha_*)\sqrt{\frac{|\alpha_*|}{a}}\left|\dot{\varepsilon}^\mathrm{p}\right|\right). \tag{16}$$

The difference in the stress–strain responses calculated by the above two backstress evolution equations, the AF model [Eq. (9)] and the present model [Eq. (16)], will be discussed in Section 3.

For the backstress evolution, the similar expressions to Eq. (12) have been used previously by several workers (e.g. Ohno and Wang, 1993; McDowell, 1995), however, the detailed formulations and features of such models are different from those of the present model. For example, Ohno and Wang (1993) proposed the following model of the backstress evolution, for an accurate description of ratchetting, at an infinitesimal deformation. The backstress $\boldsymbol{\alpha}$ consists of M component, as Chaboche and Rousselier (1983) assumed:

$$\boldsymbol{\alpha} = \sum_{i=1}^{M}\boldsymbol{\alpha}_i. \tag{17}$$

The evolution equation for each backstress component is expressed by the equation:

$$\dot{\boldsymbol{\alpha}}_i = C_i\left[\frac{2}{3}a_i\dot{\boldsymbol{\varepsilon}}^\mathrm{p} - \left(\frac{\bar{\alpha}_i}{r_i}\right)^{\gamma_i}\left\langle\dot{\boldsymbol{\varepsilon}}^\mathrm{p} : \mathbf{n}_i\right\rangle\boldsymbol{\alpha}_i\right], \tag{18}$$

where C_i, a_i, r_i and γ_i are material constants, $\dot{\boldsymbol{\varepsilon}}^{\mathrm{p}}$ stands for the plastic strain rate, and $\mathbf{n}_i = \boldsymbol{\alpha}_i/\bar{\alpha}_i$. It is well known that the AF model always gives an overestimation of ratchet–strain accumulations since the dynamic recovery of the backstress is too active. Therefore, they modified the AF model in such a way that the dynamic recovery term becomes active only when $\dot{\boldsymbol{\varepsilon}}_i^{\mathrm{p}} : \mathbf{n}_i \geqslant 0$. The threshold term $\langle \dot{\boldsymbol{\varepsilon}}^{\mathrm{p}} : \mathbf{n}_i \rangle$ in Eq. (18) plays an important role to suppress the ratchetting. On the other hand, in such a threshold model, a certain number of $\boldsymbol{\alpha}_i$ components ($M \geqslant 4$) are necessary for reproducing realistic shapes of stress–strain hysteresis loops. A serious problem there is a numerous number of material parameters.

In contrast, the present model has only one backstress evolution equation, since it excludes the threshhold term $\langle \dot{\boldsymbol{\varepsilon}}^{\mathrm{p}} : \mathbf{n}_i \rangle$. Nevertheless, as will be discussed in Section 3.1, it can describe the behavior of the transient Bauschinger effect more accurately than the AF model. The description of the ratchetting, which is a secondary effect of cyclic plasticity (as far as sheet metal forming applications are concerned), is out of scope of the present model.

2.3. Mixed isotropic–kinematic hardening of the bounding surface

For the isotropic hardening of the bounding surface, the following evolution equation is assumed:

$$\dot{R} = m(R_{\mathrm{sat}} - R)\dot{p} \tag{19}$$

where R_{sat} is the saturated value of the isotropic hardening stress R at infinitely large plastic strain, and m is a material parameter that controls the rate of isotropic hardening.

For the kinematic hardening of the bounding surface, the following evolution equation is assumed:

$$\overset{\circ}{\boldsymbol{\beta}} = m\left(\frac{2}{3} b\mathbf{D}^{\mathrm{p}} - \boldsymbol{\beta}\dot{p}\right), \tag{20}$$

where b denotes a material parameter. Here, parameter m is assumed to be the same as in the evolution equation of the isotropic hardening stress [in Eq. (19)]. It should be noted that in uniaxial tension the bounding stress yields:

$$\sigma_{\mathrm{bound}}^{(\mathrm{fow})} = B + R + \beta = B + (R_{\mathrm{sat}} + b)(1 - \mathrm{e}^{-m\varepsilon^{\mathrm{p}}}). \tag{21}$$

As Chaboche and Rousselier (1983) already pointed out, the two-surface model is generally identical with the model of superposition of two NLK components. From this point of view, the present model can also be considered as a model of superposition of two NLK components, $\boldsymbol{\alpha} = \boldsymbol{\alpha}_* + \boldsymbol{\beta}$, with an evolution of $a = B + R - Y$ [refer to Eq. (7b)].

2.4. Modeling of isotropic-hardening stagnation

The experimentally obtained stress–strain curves on a mild steel (Yoshida et al., 2001) exhibit apparent workhardening stagnation in a certain period of reverse deformation starting from the reverse re-yielding. This phenomenon is also related to the cyclic strain-range, as well as mean-strain, dependencies of cyclic hardening characteristics.

As already mentioned in Section 2.1, the workhardening stagnation is caused by the dissolution of dislocation cell walls during a reverse deformation. It can be expressed by the non-isotropic hardening (non-IH) of the bounding surface, since in the present model the isotropic hardening of the bounding surface represents the global workhardening due to the formation of stable dislocation structures, such as cell walls. We define a non-IH surface, g_σ, in the stress space, as schematically illustrated in Fig. 3(a) and (b), as

$$g_\sigma(\mathbf{s}, \mathbf{q}, r) = \frac{3}{2}(\mathbf{s} - \mathbf{q}) : (\mathbf{s} - \mathbf{q}) - r^2 = 0 \tag{22}$$

where $\mathbf{q}$ and r denote the center and the radius of the non-IH surface, respectively. We assume that the center of the bounding surface, $\boldsymbol{\beta}$, exists either on or inside of the surface g_σ. The isotropic hardening of the bounding surface takes place only when the center point of the bounding surface, $\boldsymbol{\beta}$, stays on the surface g_σ [see Fig. 3(b)], namely $\dot{R} > 0$ when

$$\begin{aligned} &g_\sigma(\boldsymbol{\beta}, \mathbf{q}, r) = \frac{3}{2}(\boldsymbol{\beta} - \mathbf{q}) : (\boldsymbol{\beta} - \mathbf{q}) - r^2 = 0 \quad \text{and} \\ &\frac{\partial g_\sigma(\boldsymbol{\beta}, \mathbf{q}, r)}{\partial \boldsymbol{\beta}} : \mathring{\boldsymbol{\beta}} = (\boldsymbol{\beta} - \mathbf{q}) : \mathring{\boldsymbol{\beta}} > 0, \end{aligned} \tag{23a}$$

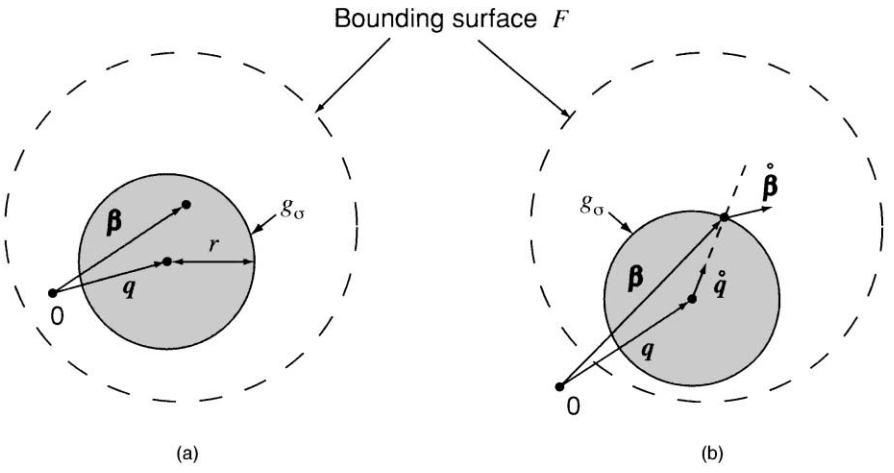

Fig. 3. Schematic illustrations of the non-IH surface g_σ defined in the stress space, when (a) non-IH ($\dot{R} = 0$); and (b) IH takes place ($\dot{R} > 0$).

$$\dot{R} = 0, \text{ otherwise.} \tag{23b}$$

From some experimental data of stress–strain curves under a large-strain reverse deformation (e.g. Christodoulou et al., 1986; Hu et al., 1992), it is found that the plastic strain region of workhardening stagnation increases with the accumulated plastic strain. Such a phenomenon can be expressed by the expansion of the surface g_σ with increasing plastic strain. Here, we assume the kinematic motion of the surface g_σ such that the center of g_σ moves in the direction of $(\boldsymbol{\beta} - \mathbf{q})$, as

$$\overset{\circ}{\mathbf{q}} = \mu(\boldsymbol{\beta} - \mathbf{q}). \tag{24}$$

From the consistency condition that the center point of the bounding surface, $\boldsymbol{\beta}$, should be either on or inside of g_σ, we have

$$\mu = \frac{3(\boldsymbol{\beta} - \mathbf{q}) : \overset{\circ}{\boldsymbol{\beta}}}{2r^2} - \frac{\dot{r}}{r}. \tag{25}$$

Here, we assume the following evolution equation for r:

$$\dot{r} = h\Gamma, \quad \Gamma = \frac{3(\boldsymbol{\beta} - \mathbf{q}) : \overset{\circ}{\boldsymbol{\beta}}}{2r} \quad \text{when} \quad \dot{R} > 0 \tag{26a}$$

$$\dot{r} = 0 \quad \text{when} \quad \dot{R} = 0. \tag{26b}$$

where h $(0 \leqslant h \leqslant 1)$ denotes a material parameter that determines the rate of expansion of surface g_σ. Then, Eq. (25) is rewritten by the equation:

$$\mu = \frac{(1-h)\Gamma}{r} \tag{27}$$

The larger value of h gives a rapid expansion of the non-IH surface, and as a result, it leads to the prediction of smaller cyclic hardening. Since the non-IH (workhardening stagnation) appears during reverse deformation after prestrain, the initial value of r may be assumed to be zero.

For the uniaxial case, the criterion for the isotropic hardening evolution is given as follows:

$$\dot{R} > 0 \text{ when } g_\sigma = (\beta - q)^2 - r^2 = 0 \text{ and } (\beta - q)\dot{\beta} > 0, \tag{28a}$$

$$\dot{R} = 0, \text{ otherwise} \tag{28b}$$

Since $\Gamma = \operatorname{sgn}[(\beta - q)\dot{\beta}]$ and $r = |\beta - q|$, the evolution equations for q and r are written by the equations:

$$\dot{q} = (1-h)\dot{\beta} \tag{29}$$

$$\dot{r} = h\left|\dot{\beta}\right| \quad \text{when} \quad \dot{R} = 0 \tag{30a}$$

$$\dot{r} = 0 \quad \text{when} \quad \dot{R} = 0 \tag{30b}$$

For an infinitesimal deformation, Chaboche et al. (1979) presented an idea of non-isotropic-hardening (non-IH) region in the plastic strain space, instead of the stress space, and Ohno (1982) proposed its generalized form. If a linear kinematic hardening of the bounding surface is assumed, we can show that the above-proposed non-IH-surface g_σ defined in the stress space is directly related to Chaboche–Ohno's non-IH-region g_ε defined in the plastic strain space, as follows. According to Ohno's (1982) formulation, the non-IH region in the plastic strain space, g_ε, is expressed by the equation:

$$g_\varepsilon(\boldsymbol{\varepsilon}^{\mathrm{p}}, \boldsymbol{\zeta}, \kappa) = \frac{2}{3}(\boldsymbol{\varepsilon}^{\mathrm{p}} - \boldsymbol{\zeta}) : (\boldsymbol{\varepsilon}^{\mathrm{p}} - \boldsymbol{\zeta}) - \kappa^2 = 0 \tag{31a}$$

$$\boldsymbol{\varepsilon}^{\mathrm{p}} = \int \dot{\boldsymbol{\varepsilon}}^{\mathrm{p}} \mathrm{d}t \tag{31b}$$

where $\boldsymbol{\zeta}$ and κ denote the center and the radius of the surface, respectively. Here, it should be noted that it is hardly possible to apply the model of non-IH plastic strain region directly to large-strain cyclic plasticity problems, because, theoretically, we cannot define the Cartesian plastic strain space when large shear deformation occurs [in other words, Eq. (31b) has no longer clear physical meaning]. The plastic strain point, $\boldsymbol{\varepsilon}^{\mathrm{p}}$, in the strain space exists either on or inside of g_ε, and the isotropic hardening takes place only when the current point stays on the surface, which is given by the equations:

$$\dot{R} > 0 \quad \text{when}$$

$$g_\varepsilon(\boldsymbol{\varepsilon}^{p}, \boldsymbol{\zeta}, \kappa) = 0 \quad \text{and} \quad \frac{\partial g_\varepsilon}{\partial \boldsymbol{\varepsilon}^{\mathrm{p}}} : \dot{\boldsymbol{\varepsilon}}^{\mathrm{p}} = (\boldsymbol{\varepsilon}^{\mathrm{p}} - \boldsymbol{\zeta}) : \dot{\boldsymbol{\varepsilon}}^{\mathrm{p}} > 0 \tag{32a}$$

$$\dot{R} = 0, \quad \text{otherwise} \tag{32b}$$

By defining

$$\Gamma_\varepsilon = \frac{2(\boldsymbol{\varepsilon}^{\mathrm{p}} - \boldsymbol{\zeta}) : \dot{\boldsymbol{\varepsilon}}^{\mathrm{p}}}{3\kappa}, \tag{33}$$

the evolution equations for $\boldsymbol{\zeta}$ and κ are written as follows:

$$\dot{\boldsymbol{\zeta}} = \mu_\varepsilon(\boldsymbol{\varepsilon}^{\mathrm{p}} - \boldsymbol{\zeta}), \quad \mu_\varepsilon = \frac{(1-h_\varepsilon)\Gamma_\varepsilon}{\kappa} \tag{34}$$

$$\dot{\kappa} = h_\varepsilon \Gamma_\varepsilon \quad \text{when} \quad \dot{R} > 0; \tag{35a}$$

$$\dot{\kappa} = 0 \quad \text{when} \quad \dot{R} = 0 \tag{35b}$$

where h_ε denotes a material parameter that determines the rate of expansion of surface g_ε.

For an infinitesimal deformation, if we assume the linear kinematic hardening of the bounding surface:

$$\dot{\boldsymbol{\beta}} = \frac{2}{3} H'_{\mathrm{Lk}} \dot{\boldsymbol{\varepsilon}}^{\mathrm{p}}, \quad \boldsymbol{\beta} = \frac{2}{3} H'_{\mathrm{Lk}} \boldsymbol{\varepsilon}^{\mathrm{p}}, \tag{36}$$

we can easily derive the following linear relationships between the variables defined in the stress space and those defined in the plastic strain space.

$$\dot{\mathbf{q}} = \frac{2}{3} H'_{\mathrm{Lk}} \dot{\boldsymbol{\zeta}}, \quad \mathbf{q} = \frac{2}{3} H'_{\mathrm{Lk}} \boldsymbol{\zeta} \tag{37a}$$

$$r = H'_{\mathrm{Lk}} \kappa, \quad \Gamma = H'_{\mathrm{Lk}} \Gamma_\varepsilon, \quad \mu = \mu_\varepsilon. \tag{37b}$$

Therefore, it is concluded that, for an infinitesimal deformation, the above two formulations for the non-IH regions are identical when linear kinematic hardening of the bounding surface is assumed.

2.5. Material parameter identification

The present model involves seven material parameters (Y, C, B, R_{sat}, b, m, h). These parameters can be systematically identified from uniaxial stress–strain curves under a cyclic deformation. The scheme of the present material parameter identification is indicated as follows.

a. The radius of yield surface Y is determined as the elastic limit.
b. From a forward-reverse stress–strain curve, we can easily draw lines of the forward and reverse bounds, $\sigma^{(\mathrm{fow})}_{\mathrm{bound}}$ and $\sigma^{(\mathrm{rev})}_{\mathrm{bound}}$, as schematically illustrated in Fig. 2(a) (lines (b)–(c) for forward deformation and (j)–(f)–(g) for reverse deformation). By fitting the line of the forward bound $\sigma^{(\mathrm{fow})}_{\mathrm{bound}}$ calculated by Eq. (21) to thus determined one, parameters B, $(R_{\mathrm{sat}} + b)$ and m will be found.
c. Parameter b is determined as follows. From Eq. (20), the permanent softening at the beginning of reverse deformation [at $\hat{\varepsilon}^{\mathrm{p}} = 0$ in Fig. 2(a)], $\sigma^{(\mathrm{p})}_{\mathrm{Bo}}$ is given by the equation:

$$\sigma^{(\mathrm{p})}_{\mathrm{Bo}} = 2\beta_{\mathrm{o}} = 2b(1 - \mathrm{e}^{-m\varepsilon^{\mathrm{p}}_{\mathrm{o}}}), \tag{38}$$

where β_{o} denotes the kinematic hardening of the bounding surface at the stress reversal point, and $\varepsilon^{\mathrm{p}}_{\mathrm{o}}$ is the plastic prestrain. Since we already have parameter m in step (a), using the experimentally obtained $\sigma^{(\mathrm{p})}_{\mathrm{Bo}}$, we can identify parameter b from Eq. (38).

Alternatively, we may also use the following equation expressing the reverse bound in the region of workhardening stagnation:

$$\sigma_{\text{bound}}^{(\text{rev})} = -(B + R_{\text{o}}) + \beta^{(\text{rev})}, \tag{39a}$$

$$R_{\text{o}} = R_{\text{sat}}(1 - e^{-m\varepsilon_{\text{o}}^{\text{p}}}), \quad \beta^{(\text{rev})} = b\left[-1 + 2e^{-m\hat{\varepsilon}^{\text{p}}} - \mathrm{e}^{-m(\varepsilon_{\text{o}}^{\text{p}} + \hat{\varepsilon}^{\text{p}})}\right]. \tag{39b}$$

Using the value of $(R_{\text{sat}} + \text{b})$ already determined in the above step (b), we can identify parameter b from Eq. (39) so as to obtain the best-fit to the experimentally determined reverse bound.

d. Parameter C is identified from the stress–strain curve of the transient Bauschinger deformation. From Eq. (16), for reverse deformation after large forward prestrain, we have

$$C \approx \frac{2}{\hat{\varepsilon}^{\text{p}}}\left[(1 + \ln 2) - \sqrt{\frac{|\alpha_*|}{a}} + \ln\left(1 + \text{sgn}(\alpha_*)\sqrt{\frac{|\alpha_*|}{a}}\right)\right]. \tag{40}$$

Since $\sigma_{\text{B}}^{(\text{t})} = a + \alpha_*$, α_*/a is given as a function of the transient stress offset $\sigma_{\text{B}}^{(\text{t})}$ as:

$$\frac{\alpha_*}{a} \approx \frac{\sigma_{\text{B}}^{(\text{t})}}{a_{\text{o}}} - 1 = 2\left(\frac{\sigma_{\text{B}}^{(\text{t})}}{\sigma_{\text{Bo}}^{(\text{t})}}\right) - 1, \quad a_{\text{o}} = \frac{1}{2}\sigma_{\text{Bo}}^{(\text{t})} = \sigma_{\text{o}} - Y - \frac{1}{2}\sigma_{\text{Bo}}^{(\text{p})}, \tag{41}$$

we can easily calculate the relationship between $\hat{\varepsilon}^{\text{p}}$ and $\sigma_{\text{B}}^{(\text{t})}/\sigma_{\text{Bo}}^{(\text{t})}$. The calculated $\hat{\varepsilon}^{\text{p}}$ vs. $\sigma_{\text{B}}^{(\text{t})}/\sigma_{\text{Bo}}^{(\text{t})}$ curves for various values of C, together with the experimental results for a mild steel and a high-strength steel (Yoshida et al., 2001), are illustrated in Fig. 4.

e. Now there remains only a parameter h. This will be identified either from the experimental data of plastic strain range of workhardening stagnation or cyclic hardening characteristics. For example, Fig. 5(a) and (b) demonstrate how strongly parameter h affects the calculated stress–strain responses under cyclic deformation. Generally speaking, a larger value of h gives the prediction of smaller saturated stress amplitudes. Parameter h is identified by the numerical simulation of such cyclic stress–strain responses so as to obtain the best-fit curves to the corresponding experimental results.

Instead of the above scheme for the material parameter identification, it is also possible to determine the set of material parameters (Y, C, B, R_{sat}, b, m, h) simultaneously by using an optimization technique (e.g. Toropov et al., 1993; Yoshida et al., 1998, 2000; also see the Appendix).

3. Performance of the model

3.1. Comparison of numerical simulations and experimental results

Numerical simulations of stress–strain responses were conducted using the present model (termed 'Yoshida–Uemori model'). The calculated results were compared to

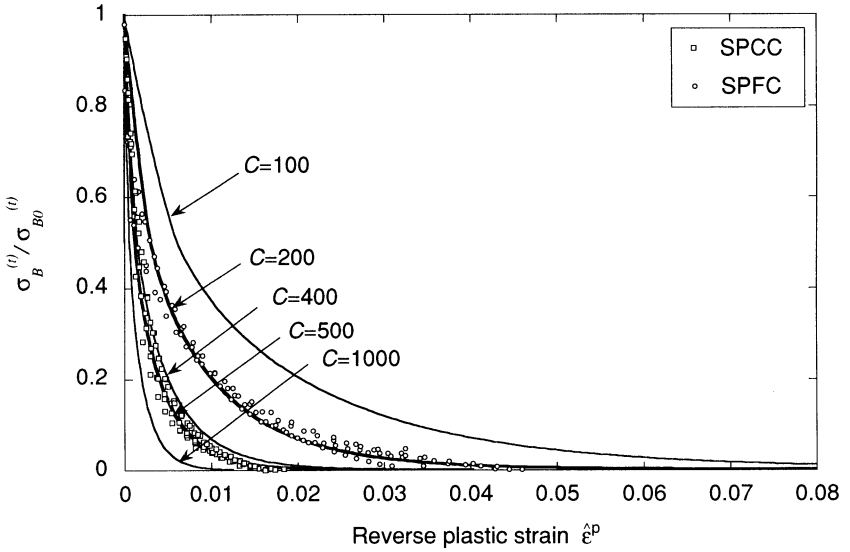

Fig. 4. Normalized transient stress offset $\sigma_B^{(t)}/\sigma_{Bo}^{(t)}$ as a function of reverse plastic strain $\hat{\varepsilon}^p$ for various values of parameter C. Experimental data on a mild steel sheet (SPCC) and a high strength steel sheet (SPFC) have been taken from a paper by Yoshida et al. (2001).

the corresponding experimental data for mild steel and high strength steel sheets under in-plane cyclic tension–compression (Yoshida et al., 2001). In the simulation, the effect of plastic strain, $p = \int \dot{p} \mathrm{d}t$, on Young's moduli, E, was taken into account using the following empirical equation (Yoshida et al., 2001):

$$E = E_o - (E_o - E_a)[1 - \exp(-\xi p)], \tag{42}$$

where E_o and E_a stand for Young's modulus for virgin and infinitely large pre-strained materials, respectively, and ξ is a material constant. The identified values of sets of material parameters for plasticity (Y, C, B, R_{sat}, b, m, h) as well as the parameters for Young's moduli (E_o, E_a, ξ) for both steel sheets, are listed in Table 1.

In order to examine the difference in the performance of describing the cyclic stress–strain responses between the present model and a typical classical model, the numerical simulations were also conducted using the IH + NLK model. The details of the IH + NLK model are indicated in Table 2.

Fig. 6(a) and (b) show the effective stress vs. strain ($|\sigma|$ vs. $|\varepsilon|$) under a monotonic loading and reverse deformations, calculated by the present model, for the mild steel and the high strength steel, respectively, together with the experimental results. The calculated results by the IH + NLK model are depicted in Fig. 7(a) and (b). For both steels, the present model gives much better results than the IH + NLK model. Especially for the case of mild steel sheet, the present model well describes the behavior of workhardening stagnation, while the IH + NLK model cannot. As already mentioned in the Introduction, abnormal shapes of reverse stress–strain curves due to the

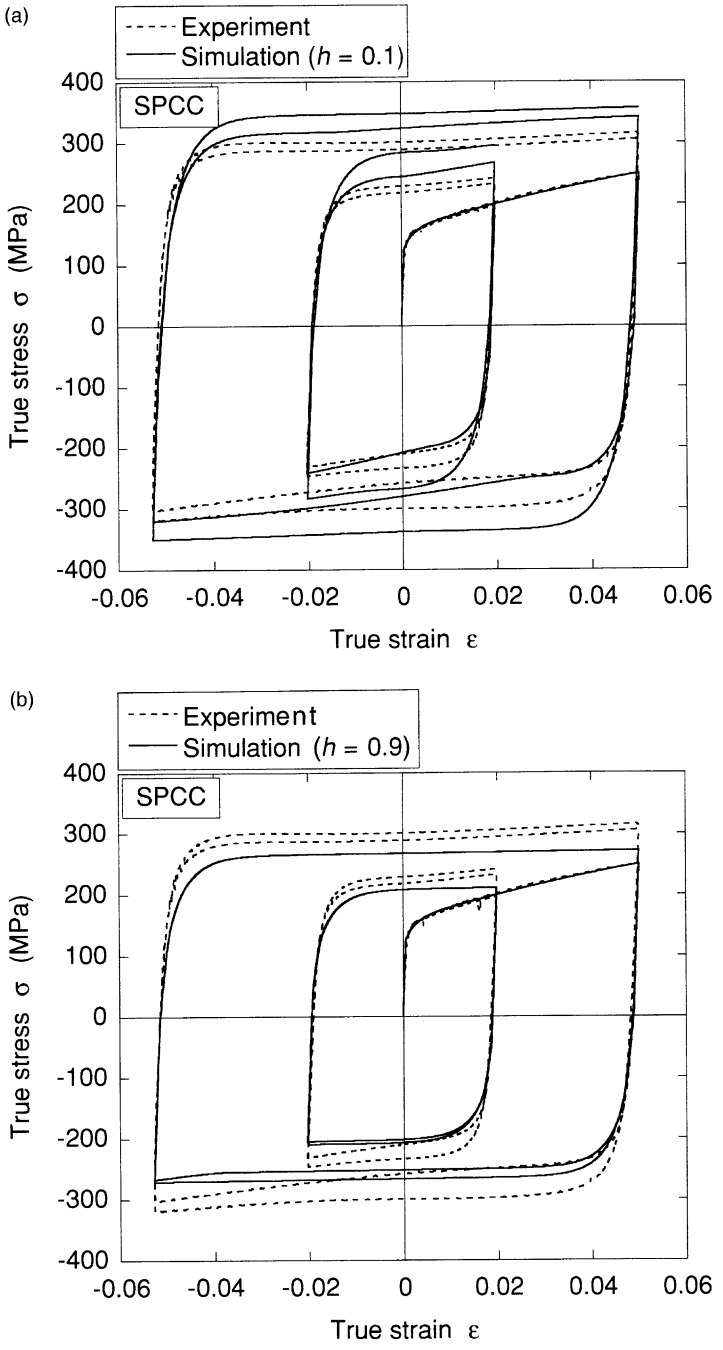

Fig. 5. Effect of parameter h on the simulation of cyclic stress–strain responses: (a) $h=0.1$; (b) $h=0.9$. The other material parameters are $Y=124$ MPa, $C=500$, $B=168$ MPa, $R_{sat}=190$ MPa, $b=9.0$, $m=12.0$.

Table 1
Material parameters in Yoshida–Uemori model

	Plasticity parameters							Parameters for prestrain dependent Young's moduli		
	Y (MPa)	C	B (MPa)	R_{sat} (MPa)	b (MPa)	m	h	E_0 (GPa)	E_a	ξ
SPCC	124	500	168	190	9	12	0.5	206	152	30.8
SPCC	360	200	435	255	66	26	0.4	206	159	61.0

Table 2
A mixed isotropic-kinematic hardening model (IH + NLK model)

• The yield function and the associated flow rule

$$f=\frac{3}{2}(\mathbf{s}-\boldsymbol{\alpha}):(\mathbf{s}-\boldsymbol{\alpha})-(Y+R)^2=0,\quad \mathbf{D}^{\mathrm{p}}=\frac{\partial f}{\partial \mathbf{s}}\dot{\lambda}.$$

• Isotropic hardening (IH) rule

$$\dot{R}=m(R_{\mathrm{sat}}-R)\dot{p}.$$

• Nonlinear kinematic hardening (NLK) rule

$$\mathring{\boldsymbol{\alpha}}=C\left(\frac{2}{3}a\mathbf{D}^{\mathrm{p}}-\boldsymbol{\alpha}\dot{p}\right).$$

$[Y,\ R_{\mathrm{sat}},\ m,\ C,\ a]$ = material parameters

workhardening stagnation appear only on the mild steel, but not on the high strength sheet. About this point, it should be noted that the present model also predicts stress–strain responses with apparent workhardening stagnation only on the mild steel. This is because the high strength steel has less strong isotropic hardening nature than the mild sheet, and as a result, the workhardening stagnation behavior is not visible in the calculated stress–strain curves, despite the inclusion of the non-IH region in the model. This explanation is not only for the modeling but also for real material behavior. The strain-range and mean-strain dependencies of cyclic hardening characteristics are also well reproduced by the present model, owing to the non-IH surface modeling, as shown in Fig. 8(a) and (b) for the mild steel and in Fig. 9 for the high strength steel. In Fig. 9, the calculated results include a modification for material parameter C, which will be discussed in the next section of this paper.

As well as the global cyclic hardening behavior, it is very important to simulate precisely the transient Bauschinger deformation, especially for the purpose of accurate prediction of springback in sheet metal forming simulations. The stress–strain responses during the transient period calculated by the two models are quite different as can be seen from Fig. 10. This is mainly due to the difference in the backstress evolution equations between the AF model [for uniaxial case, Eq. (9)] and the present model [Eq. (16)]. From Fig. 10, it can be concluded that the backstress evolution Eq. (16) is the better choice than the AF model.

The proposed constitutive model is highly capable of describing cyclic stress–strain responses at large strain, not only for steels but also for most metallic materials.

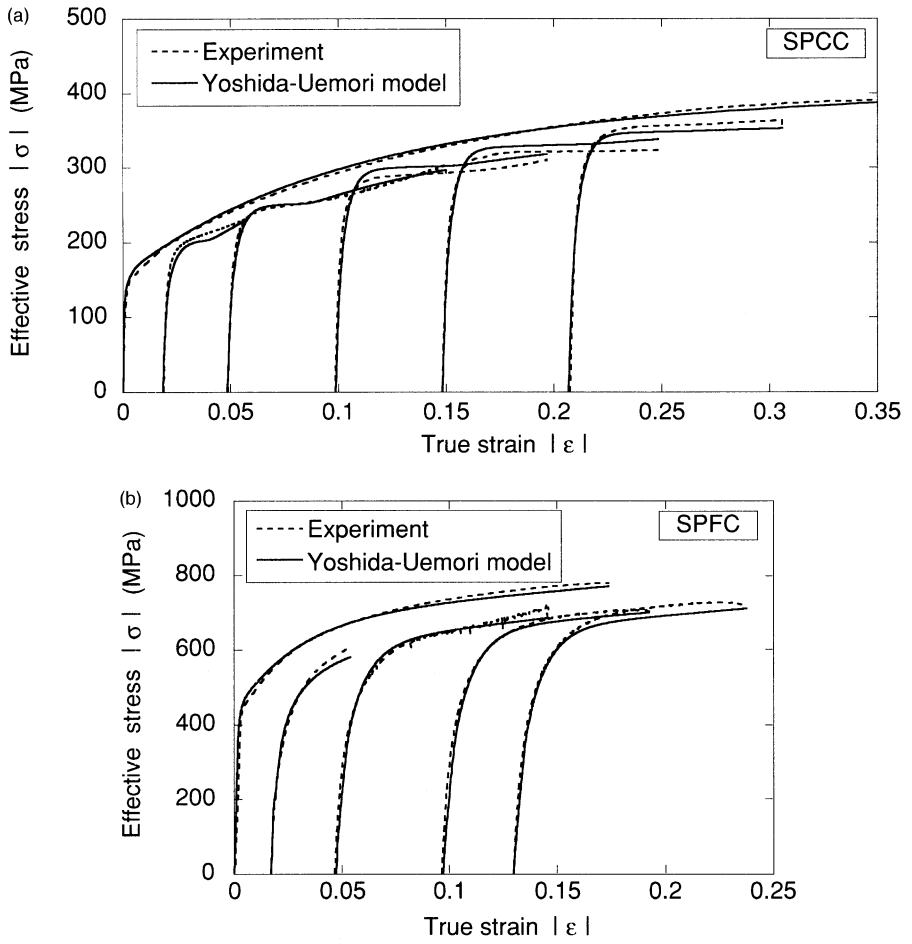

Fig. 6. Effective stress vs. strain curves under reverse deformations calculated by Yoshida–Uemori model, together with the experimental results (Yoshida et al., 2001): (a) mild steel sheet (SPCC); (b) high strength steel sheet (SPFC). Material parameters are listed in Table 1.

For example, Fig. 11 depicts the comparison of the effective stress vs. strain curves for 5083 aluminum sheet calculated by the present model and the experimental data reported by Kuwabara et al. (1995). From this figure, it is found that the aluminum alloy has a characteristic of larger permanent softening compared to steels, and even for such a case, this model can well simulate the material behavior.

3.2. Some modifications of the model

The above proposed model uses the same kinematic hardening rules with fixed material parameters both for the forward and reverse deformations based on the assumption that the shape of the stress–strain curve of forward deformation is closely

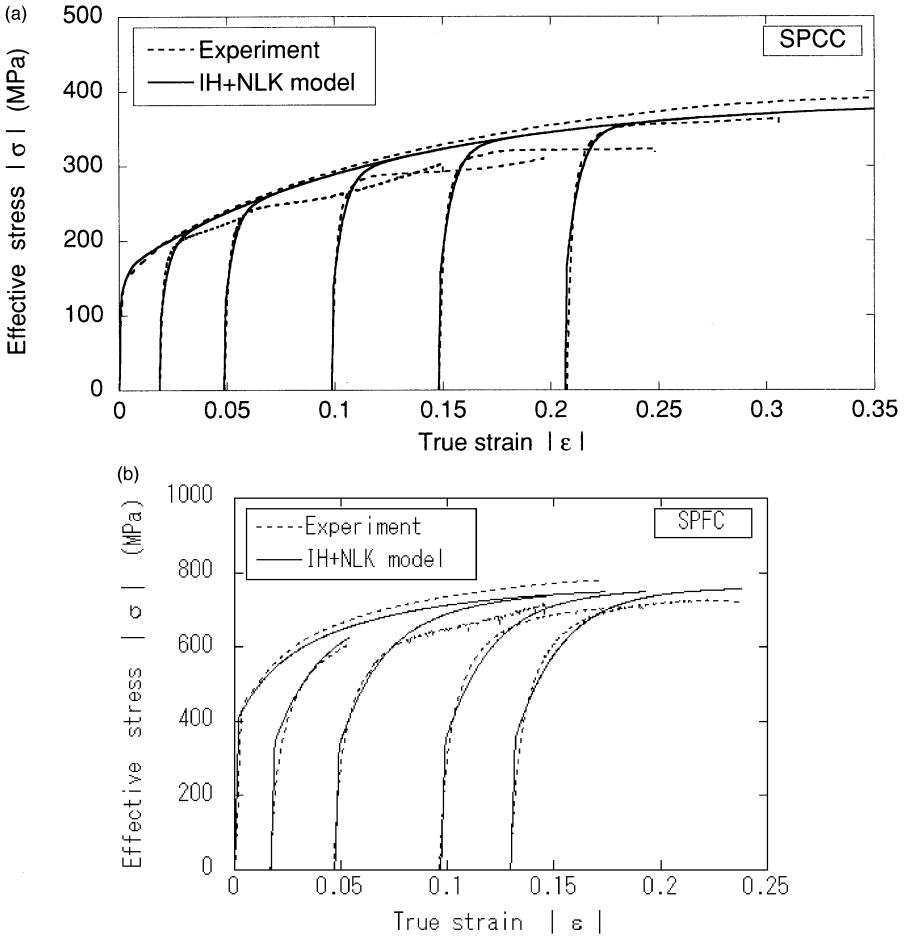

Fig. 7. Effective stress vs. strain curves under reverse deformations calculated by the IH + NLK model: (a) mild steel sheet (SPCC, $Y = 120$ MPa; $C = 390$; $a = 43$ MPa; $R_{sat} = 166$ MPa and $m = 8.4$); (b) high strength steel sheet (SPFC, $Y = 410$ MPa; $C = 70$; $a = 144$ MPa; $R_{sat} = 157$ MPa and $m = 16.0$).

related to one of reverse deformation. Although this assumption has been also accepted by most of existing models (e.g. Mroz, 1967; Chaboche and Rousselier, 1983; Ohno and Wang, 1993; Hu, 1994), in reality, it may be too rough. For most of cases, the change of workhardening rate after the initial yielding is not so slow as the model predicts (see Fig. 12, as an example). In order to solve the problem one of the present authors and his co-workers (Yoshida et al., 1998) made a simple modification in the AF model such that the material parameter C takes two different values C_1 and C_2 for forward and reverse deformations, respectively. As a similar idea, one of the easiest way of the modification of the present model to describe more rapid change of workhardening rate in the vicinity of initial yielding, we may introduce the following auxiliary rule for material parameter C:

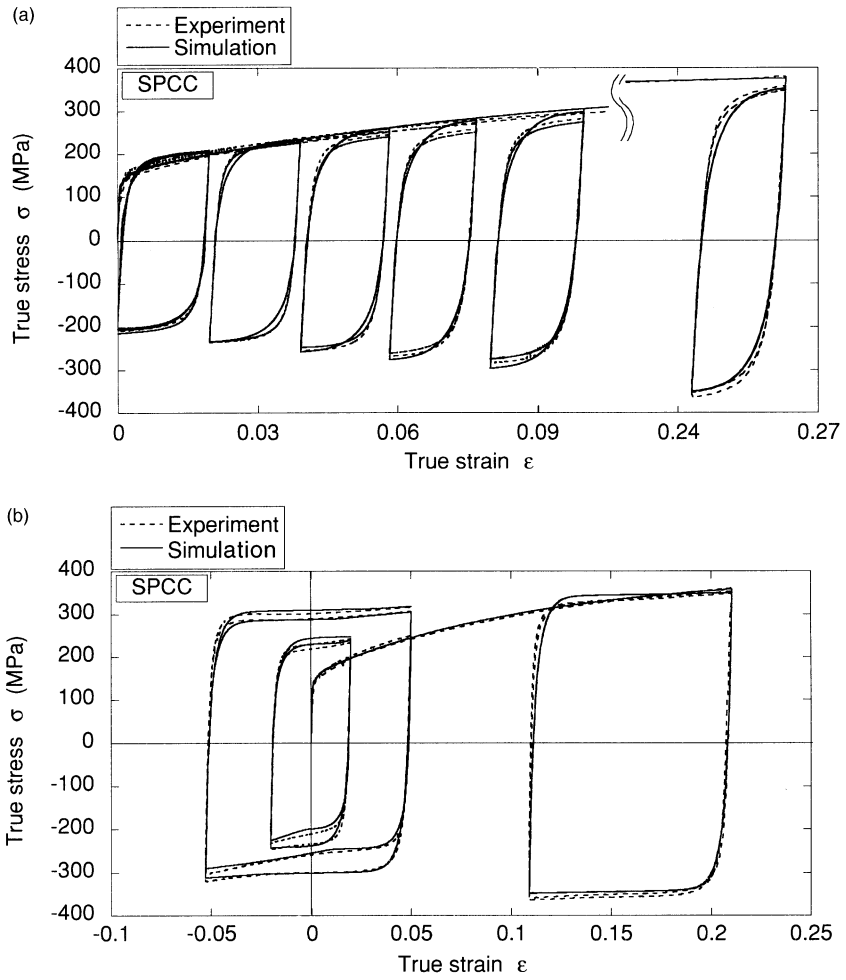

Fig. 8. Cyclic stress–strain responses of a mild steel sheet (SPCC) under cyclic deformations calculated by Yoshida–Uemori model, together with the experimental results (Yoshida et al., 2001): (a) cyclic straining of strain range of 0.02 with various mean strains; (b) various types of cyclic straining including large strain range of 0.10.

$$C = C_1 \quad \text{when} \quad \mathrm{Max}(\bar{\alpha}_*) < B - Y, \tag{43a}$$

$$C = C_2, (C_1 > C_2), \quad \text{otherwise}, \tag{43b}$$

where $\mathrm{Max}(\bar{\alpha}_*)$ is the maximum value of $\bar{\alpha}_*$. For example, if we choose $C_1 = 2000$ and $C_2 = 200$ for the high strength sheet, instead of $C = 200$ for both forward and reverse deformations, the calculated stress–strain curve in the vicinity of initial yielding becomes more realistic, as shown in Fig. 12.

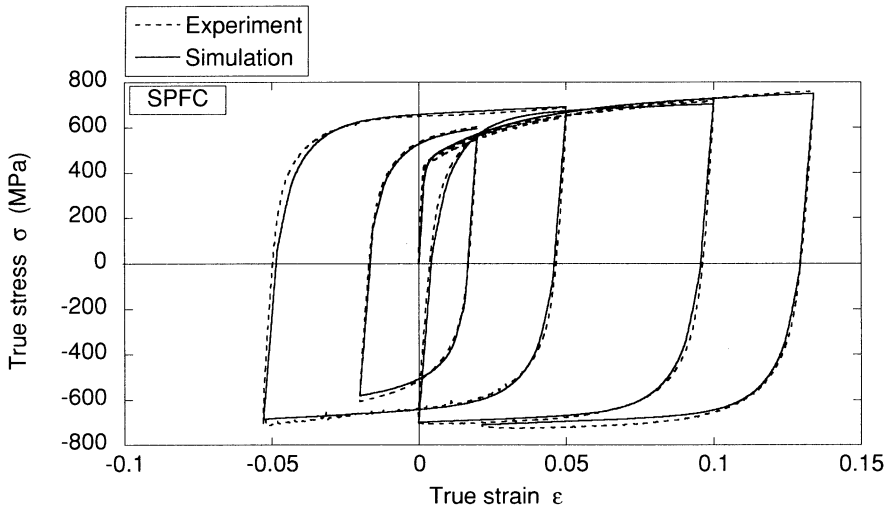

Fig. 9. Cyclic stress–strain responses of high strength steel sheet (SPFC) under various cyclic deformations calculated by Yoshida–Uemori model, together model with the experimental results (Yoshida et al., 2001). The model includes a modification for material prameter C [$C_1 = 2000$ and $C_2 = 200$ in Eq. (43)].

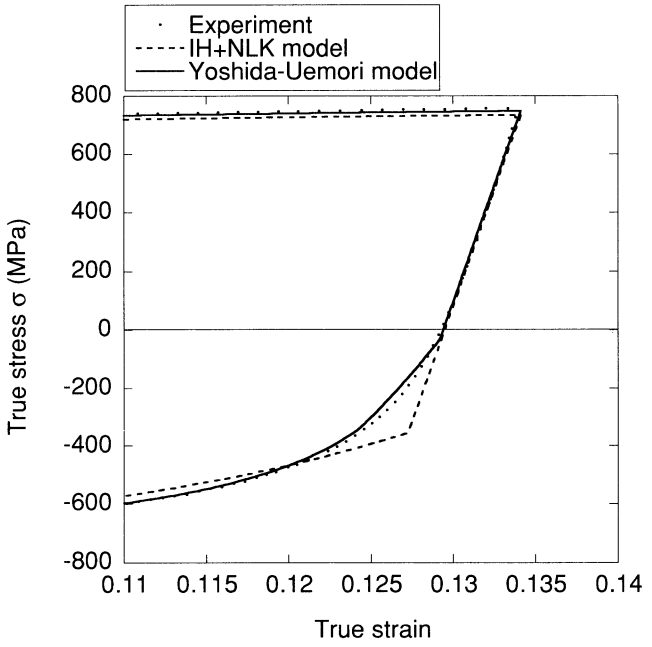

Fig. 10. Stress–strain responses during the transient Bauschinger deformation calculated by Yoshida–Uemori model and the IH + NLK model, together with the experimental results. Material parameters for Yoshida–Uemori model are listed in Table 1, and for IH + NLK model are shown in the caption of Fig. 7.

As an extreme case where the shapes of stress–strain curves between forward and reverse deformations are completely different, we may pick up the yield-point phenomena often observed on annealed steels and some aluminum alloys (e.g. see Fig. 13 on a mild steel sheet). If we intend to describe precisely the yield-point phenomena,

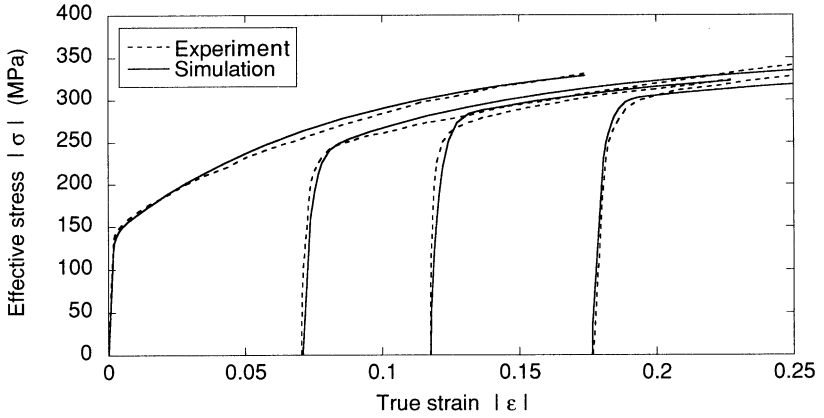

Fig. 11. Stress–strain responses of 5083 aluminum sheet under reverse deformations calculated by Yoshida–Uemori model, together with the experimental results reported by Kuwabara et al. (1995). Material parameters are $Y=80$ MPa; $C=900$; $B=140$ MPa; $R_{\text{cat}}=180$ MPa; $b=22.0$; $m=13.0$ and $h=0.001$.

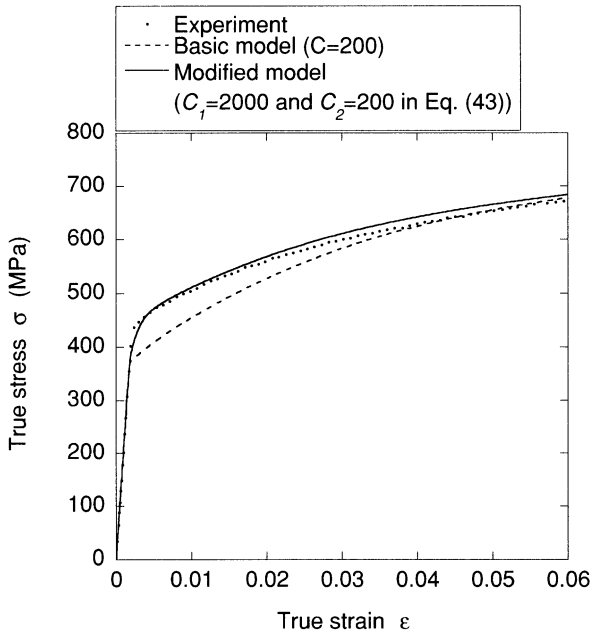

Fig. 12. Stress–strain curve of high strength steel (SPFC) in the vicinity of initial yielding. Predictions by the basic version of Yoshida–Uemori model and the modified version with Eq. (43) are illustrated. Material parameters (except C) are listed in Table 1.

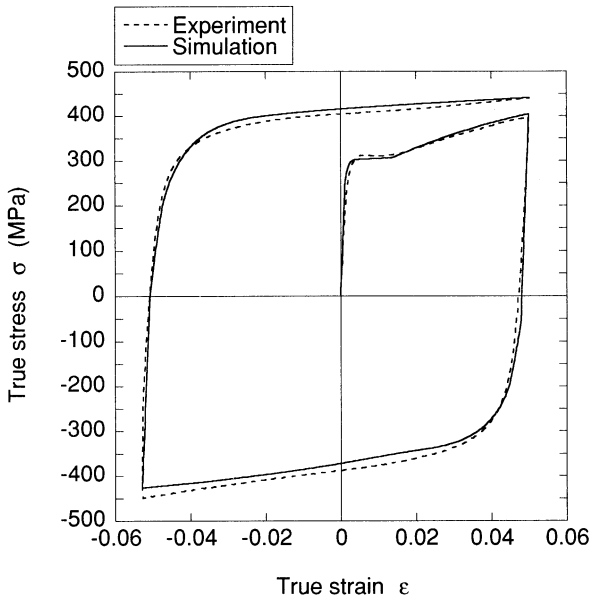

Fig. 13. Stress–strain responses including yield-plateau on a mild steel sheet and its prediction by Yoshida–Uemori model. Material parameters are $Y=200$ MPa; $C=220$; $B=304$ MPa, $R_{\text{sat}}=165$ MPa, $b=10.0$, $m=25.0$; $h=0.8$ and $r_{\text{initial}}=3.0$ MPa.

we should have a physically based constitutive model. One of the present author (Yoshida, 2000) recently proposed a viscoplasticity constitutive model of cyclic plasticity that describes the sharp yield point and the subsequent abrupt yield drop on the premise that the yield-point phenomena are attributed to the rapid dislocation multiplication and the stress-dependence of dislocation velocity. Instead of such a physically based model, here we introduce a simple modification of the present model for the description of the yield-plateau in the stress–strain curve. We assume that the bounding surface has initially non-IH nature up to a certain range of plastic deformation, namely, initial size of non-IH surface is not zero ($r=r_{\text{initial}}>0$ at $p=0$). Using this modification for non-IH surface, together with the above proposed auxiliary rule of Eq. (43), it becomes possible to simulate the yield-plateau, as shown in Fig. 13.

The texture-induced anisotropy is regarded as one of the important factors that affects the formability of sheet metals. A general form of the yield function including such anisotropy is given by the equation:

$$f=\frac{3}{2}(\mathbf{s}-\boldsymbol{\alpha}):\mathbf{M}:(\mathbf{s}-\boldsymbol{\alpha})-Y^2=0, \tag{44}$$

where $\mathbf{M}$ denotes a fourth-order tensor that describes the texture-induced anisotropy. The function for the bounding surface should be the same form:

$$F = \frac{3}{2}(\mathbf{s} - \boldsymbol{\beta}) : \mathbf{M} : (\mathbf{s} - \boldsymbol{\beta}) - (B + R)^2 = 0 \tag{45}$$

For the full description of the texture-induced anisotropy, we need further investigations on the determination of anisotropy tensor $\mathbf{M}$ and also the backstress evolution equations. For that purpose, we should have experimental data on multiaxial plasticity.

4. Concluding remarks

A constitutive model of large-strain cyclic plasticity has been presented. The validity of the present model has been confirmed by comparing the results of numerical simulations of stress–strain responses under cyclic deformation at large strain and the corresponding experimental observations on mild steel sheets, a high strength steel sheet and an aluminum alloy sheet. The highlights of this model are summarized as follows.

1. The workhardening stagnation is described by our original idea of a non-IH surface defined in the stress space. Consequently, the model can predict
   - abnormal stress–strain curves appearing in some metals under large-strain reverse deformation,
   - strain-range and mean-strain dependencies of cyclic hardening characteristics.

2. The newly proposed evolution equations for the backstress, Eqs. (14) and (15) [or for more general forms, Eqs. (12) and (13)], allow us to describe the smooth elastic-plastic transition during the transient Bauschinger deformation more realistically than when using the AF model.
3. This model involves basically seven material parameters. If we compare the number of material parameters between the present model and some other classical models (e.g. the IH + NLK and IH + NLK + LK models include five and six parameters, respectively), we can say that seven parameters are not so many. One of the advantages of this model is that the set of material parameters can be identified directly from the stress–strain curves of cyclic plasticity (this scheme has been indicated in Section 2.5).
4. This model is highly flexible in describing several types of stress–strain curves in the vicinity of initial yielding, including the yield-plateau phenomenon.

Appendix. Material parameter identification based on an optimization technique

Let $\mathbf{x} = [Y, C, B, \ldots]$ denote a set of material parameters to be identified. We will find the vector $\mathbf{x}$ that minimizes the objective function

$$F(\mathbf{x}) = \sum_{\alpha=1}^{L} \theta^{\alpha} F^{\alpha}(\mathbf{x}), \quad A_i \leqslant x_i \leqslant B_i, \quad (i = 1, 2, \ldots, N) \tag{A1}$$

where L is the total number of individual forward or reverse deformation (denoted by α). A_i and B_i are the lower and upper limits of the searching area for a material parameter x_i. $F^{\alpha}(\mathbf{x})$ is the dimensionless function defined as the square difference in stress between the experimental data, $\sigma^{\alpha}_{s(\mathrm{exp})}$, and the corresponding calculated results for an assumed set of material parameters $\mathbf{x}$, $\sigma^{\alpha}_{(\mathrm{cal})}(\mathbf{x}, \varepsilon^{\alpha}_{s})$ as

$$F^{\alpha}(\mathbf{x}) = \left\{ \sum_{s=1}^{S_\alpha} [\sigma^{\alpha}_{S(\mathrm{exp})} - \sigma^{\alpha}_{(\mathrm{cal})}(\mathbf{x}, \varepsilon^{\alpha}_{s})]^2 \right\} / \left\{ \sum_{s=1}^{S_\alpha} [\sigma^{\alpha}_{s(\mathrm{exp})}]^2 \right\}, \tag{A2}$$

where S_α is the total numbers of data points in αth stress–strain response. In Eq. (A1), θ^{α} is the weight coefficient which determines the relative contribution of αth set of experimental data. For the minimization of the objective function, we used an optimization technique based on the iterative multipoint concept (refer to Toropov et al., 1993; Yoshida et al., 1998, 2000).

References

Anon., 1997. Models for metals subjected to cyclic loading. In: ABAQUS Standards User's Manual, Version 5.7. Hibbit, Karlson & Sorensen, Inc., pp. 11.2.2.1–11.2.2.5.

Armstrong, P.J., Frederick, C.O., 1966. A mathematical representation of the multiaxial Bauschinger effect. GEGB report RD/B/N731. Berkeley Nuclear Laboratories.

Besdo, D., 2000. On numerical problems with the simulation of the spring back phase of sheet metal forming process. In: Khan, A.S., Zhan, H., Yuen, Y. (Eds.), Proc. 8th Int. Symp. on Plasticity and Its Current Applications, NEAT Press, pp. 17–19.

Burlet, H., Cailletetaud, G., 1987. Modeling of cyclic plasticity in finite element codes. In: Proc. of 2nd Int. Conf. on Constitutive Laws for Engineering Materials, Theory and Application, pp. 1157–1165.

Chaboche, J.L., Dang-Van, K., Cordier, G., 1979. Modelization of the Strain Memory Effect on the Cyclic Hardening of 316 Stainless Steels. SMiRT-5, Div. L, Paper No. L. 11/3.

Chaboche, J.L., Rousselier, G., 1983. On the plastic and viscoplastic constitutive equations, part I and II. ASME Journal of Pressure Vessel Technology, 105, 153–164.

Christodoulou, N., Woo, O.T., MacEwen, S.R., 1986. Effect of stress reversals on the work hardening behaviour of polycrystalline copper. Acta Metall 34, 1553–1562.

Dafalias, Y.F., Popov, E.P., 1976. Plastic internal variables formalism of cyclic plasticity. ASME J. Applied Mechanics 43, 645–651.

Dafalias, Y.F., 1985. The plastic spin. ASME J. Applied Mechanics 52, 865–871.

Dafalias, Y.F., Rashid, M.M., 1989. The effect of plastic spin on anisotropic material behavior. Int. J. Plasticity 5, 227–246.

Diegele, E., Jansohn, W., Tsakmakis, Ch., 2000. Finite deformation plasticity and viscoplasticity laws exhibiting nonlinear hardening rules, part I: constitutive theory and numerical integration. Computational Mechanics 25, 1–12.

Hasegawa, T., Yakou, T., 1975. Deformation behaviour and dislocation structures upon stress reversal in polycrystalline aluminium. Mater. Sci. Eng. 20, 267–276.

Hu, Z., Rauch, E.F., Teodosiu, C., 1992. Work-hardening behavior of mild steel under stress reversal at finite strains. Int. J. Plasticity 8, 839–856.

Hu, Z., 1994. Work-hardening behavior of mild steel under cyclic deformation at finite strains. Acta Metall. Mater. 42, 3481–3491.

Khan, A.S., Jackson, K.M., 1999. On the evolution of isotropic and kinematic hardening with finite plastic deformation, part I: compression/tension loading of OFHC copper cylinders. Int. J. Plasticity 15, 1265–1275.

Krieg, R.D., 1975. A practical two surface plasticity theory. ASME J. Applied Mechanics 42, 641–646.
Kuroda, M., 1996. Roles of plastic spin in shear banding. Int. J. Plasticity 12, 671–694.
Kuwabara, T., Morita, Y, Miyashita, Y., Takahashi, S., 1995. Elastic-plastic behavior of sheet metal subjected to in-plane reverse loading. In: Tanimura, S., Khan, A.S. (Eds.), Proc. 5th Int. Symp. on Plasticity and Its Current Applications, Gorddon and Breach, pp. 841–844.
McDowell, D.L., 1995. Stress state dependence of cyclic ratcheting behavior of two rail steels. Int. J. Plasticity 11, 397–421.
Miller, M.P., Harley, E.J., Bammann, D.J., 1999. Reverse yield experiments and internal variable evolution in polycrystalline metals. Int. J. Plasticity 15, 93–117.
Mroz, Z., 1967. On the description of anisotropic work-hardening. J. Mech. Phys. Solids 15, 163–175.
Ohno, N., 1982. A constitutive model of cyclic plasticity with a non-hardening strain range. ASME J. Applied Mechanics 49, 721–727.
Ohno, N., Wang, J.-D., 1993. Nonlinear kinematic hardening rule with critical state of dynamic recovery, part I: formulation and basic features for ratchetting behavior. Int. J. Plasticity 9, 3575–3590.
PAM-STAMP™, 2000. Version 2000 Release Notes. Mixed Kinematic-Isotropic Hardening Model, vol. 9. ESI/PSI.
Stout, M.G., Rollett, A.D., 1990. Large-strain Bauschinger effects in fcc metals and alloys. Metal. Trans. A 21A, 3201–3213.
Takahashi, H., Shiono, I., 1991. Backlash model for large deformation behavior of aluminium under torsional cyclic loading. Int. J. Plasticity 7, 199–217.
Teodosiu, C., Duval, J.-L., Haddadi, H., 1997. Modelling the microstructural evolution during large plastic deformations. In: Bruhns, O.T., Stein, E. (Eds.), Proceedings of the IUTAM Symposium on Micro- and Macrostructural Aspects of Thermoplasticity. Kluwer Academic, pp. 479–488.
Toropov, V.V., Filatov, A.A., Polynkin, A.A., 1993. Multiparameter structural optimization using FEM and multipoint explicit approximates. Structural Optimization 6, 7–14.
Uemori, T., Okada, T., Yoshida, F., 1998. Simulation of springback in V-bending process by elastoplastic finite element method with consideration of Bauschinger effect. Metals and Materials 4 (3), 311–314.
Uemori, T., Okada, T., Yoshida, F., 2000. FE analysis of spnngback in hat-bending with consideration of initial anisotropy and the Bauschinger effect. Key Engineering Materials 177–180, 497–502.
Van der Gissen, E., 1991. Micromechanical and thermodynamic aspects of the plastic spin. Int. J. Plasticity 7, 365–386.
Wagoner, R.H., Geng, L., Balakrishnan, V., 2000. Role of hardening law in springback. In: Khan, A.S., Zhan, H., Yuen, Y. (Eds.), Proc. 8th Int. Symp. on Plasticity and Its Current Applications. NEAT Press, pp. 609–611.
Wilson, D.V., Bate, P.S., 1986. Reversibility in the workhardening of spheroidised steels. Acta metall 34, 1107–1120.
Yoshida, F., Urabe, M., Toropov, V.V., 1998. Identification of material parameters in constitutive model for sheet metals from cyclic bending tests. Int. J. Mechanical Science 40, 237–249.
Yoshida, F., 2000. A constitutive model of cyclic plasticity. Int. J. Plasticity 16, 359–380.
Yoshida, F., Uemori, T., Okada, T., Toropov, V.V., 2000, Identification of material parameters in large-strain cyclic plasticity models for sheet metal forming applications. In: Khan, A.S., Zhan, H., Yuen, Y. (Eds.), Proc. 8th Int. Symp. on Plasticity and Its Current Applications. NEAT Press, pp. 612–614.
Yoshida, F., Uemori, T., Fujiwara, K., 2002. Elastic-plastic behavior of steel sheets under in-plane cyclic tension-compression at large strain. Int. J. Plasticity, 18, 633–659.
Zbib, H.M., Aifantis, E.C., 1988. On the concept of relative and plastic spin and its implimentations to large deformation theories, part I and II. Acta Mech. 75, 15.